

## Multiple regimes and low-frequency oscillations in the Southern Hemisphere's zonal-mean flow

Seongjoon Koo, Andrew W. Robertson, and Michael Ghil

Department of Atmospheric Sciences and Institute of Geophysics and Planetary Physics, University of California, Los Angeles, Los Angeles, California, USA

Received 2 October 2001; revised 20 March 2002; accepted 25 March 2002; published XX Month 2002.

[1] Multiple regimes in the atmospheric zonal-mean flow of the Southern Hemisphere are examined using 53 years of daily observational analysis data. Estimates of the probability density function in the reduced-phase space spanned by the two leading empirical orthogonal functions (EOFs) are found to exhibit significant deviations from bivariate Gaussianity. Two major regimes are identified, which describe the extreme phases of atmospheric zonal-flow vacillation: in the high-latitude regime the jet is displaced poleward from its climatological mean position, while in the low-latitude regime it is displaced equatorward. The two zonal-flow regimes are maintained by the forcing due to transient eddies against surface friction. Significant low-frequency oscillatory components, with peaks near 135 and 70 days, are found in the EOF mode associated with zonal-flow vacillation. These oscillations are described using both the multitaper method and singular spectrum analysis. Close examination of the relationship between the regimes and the oscillations suggests that the high- and low-latitude regimes tend to be associated with the extremes of either low-frequency oscillation. We illustrate how the phase information of either low-frequency oscillation could be used as a predictor for the high- and low-latitude regime.

*INDEX TERMS:* 1620 Global Change: Climate dynamics (3309); 3319 Meteorology and Atmospheric Dynamics: General circulation; 3346 Meteorology and Atmospheric Dynamics: Planetary meteorology (5445, 5739); 3364 Meteorology and Atmospheric Dynamics: Synoptic-scale meteorology; *KEYWORDS:* zonal-flow vacillation, weather regimes, intraseasonal oscillations, predictability, time series analysis, Southern Hemisphere

**Citation:** Koo, S., A. W. Robertson, and M. Ghil, Multiple regimes and low-frequency oscillations in the Southern Hemisphere's zonal-mean flow, *J. Geophys. Res.*, 107(0), XXXX, doi:10.1029/2001JD001353, 2002.

### 1. Introduction

[2] Low-frequency variability (LFV) of tropospheric midlatitude circulation in the Southern Hemisphere (SH) contains a large zonally symmetric component [Kidson, 1988, 1991; Karoly, 1990]. This is due to the limited role of topography and land-sea contrast in the SH circulation [Newton, 1972]. The leading LFV mode of the zonal-mean zonal flow in the SH thus takes the form of excursions of the zonal jet from its climatological mean position, with equivalent barotropic dipolar anomalies centered near 40°S and 60°S [Yoden *et al.*, 1987; Kidson, 1988]. Hartmann and Lo [1998] found this meridional shift of the midlatitude zonal jet to occur in irregular and abrupt fashion, without distinct periodicities.

[3] This phenomenon is known as zonal-flow vacillation or zonal-index variation. We shall use the former term in order to avoid any confusion with the zonal index, originally introduced by Rossby *et al.* [1939] to measure the strength of westerly wind in the Northern Hemisphere (NH), although Willett [1948] found that changes in the NH zonal

index are also associated with meridional shifts of the zonal jet.

[4] The fact that zonal-flow vacillation is characterized by irregular transitions between two persistent zonal-jet states suggests the framework of multiple regimes. In this framework, atmospheric LFV is characterized in terms of a small set of regions in phase space where the probability density function (PDF) attains local maxima, together with rather abrupt transitions among regions. If this framework provides a correct model for zonal-flow vacillation, bimodality associated with the two persistent zonal-jet states should be visible in a PDF distribution of the observed zonal-mean flow.

[5] There have been several efforts to identify bimodality and multiple regimes associated with zonal-flow vacillation. Yoden *et al.* [1987] studied LFV of zonal-mean flow during the 1980–1983 austral winters and found two distinct regimes that correspond to single- and double-jet states and are associated with the meridional shift of the midlatitude zonal jet. Akahori and Yoden [1997] found bimodality in a histogram plot of an empirical measure of the typical latitude of wave breaking associated with the zonal-flow vacillation in an idealized global model. No bimodality was visible, however, in a histogram of the zonal-mean flow's first principal component (PC-1).

[6] *Hartmann and Lo* [1998] also reported finding no bimodality in PC-1 of the observed zonal-mean SH flow. *Kidson and Watterson* [1999] studied zonally symmetric variability in a general circulation model and found no evidence of bimodality or multiple clusters in a univariate index of the vacillation. Evidence of multiple regimes associated with zonal-flow vacillation is thus still inconclusive.

[7] *Hartmann and Lo* [1998] did not find, moreover, a significant difference between the power spectrum of the zonal-mean flow's PC-1 and red noise, but other studies do suggest an intraseasonal time scale of the vacillation. *Kidson* [1986] studied the zonal-wind variations in the SH during the Global Weather Experiment and did find that the zonal wind vacillates between middle and high latitudes, with an average period of 27 days. From the longer 15-year sample of Australian hemispheric analyses, *Kidson* [1988] discovered that a zonal-jet vacillation with timescales of 12.5–50 days contributes significantly to transitions between single- and double-jet regimes at 60°S during the SH winter. *Kidson* [1991] analyzed daily European Center for Medium-Range Weather Forecasts data for 1980–1988 and found that the leading empirical orthogonal function (EOF-1) of 500 hPa geopotential height anomalies is associated with zonal-flow vacillation. He showed that the main contribution to this EOF comes from the intraseasonal bands peaking at 13–14 and 22–24 days.

[8] One major goal of this paper is to determine whether multiple regimes do exist in the SH's zonal-flow vacillation by applying an advanced density estimation technique to one of the most comprehensive SH analysis data sets available at the present time. The other major goal is to identify the low-frequency oscillations (LFOs), if any, that are associated with the vacillation. If they do exist, it would be interesting to know the relationship between the two different views of the LFV, that is, episodic occurrence of persistent regimes versus rather regular and predictable LFOs [*Ghil et al.*, 1991; *Ghil and Robertson*, 2002]. Such relationships have been investigated for the NH atmospheric variability by *Plaut and Vautard* [1994] and *Simonnet and Plaut* [2001], among others.

[9] The data and methodology used in this study are described in section 2. In section 3 we present detailed results of probability density estimation. Temporal behavior of the mode associated with zonal-flow vacillation is examined in section 4. Section 5 describes the relationship between multiple flow regimes and the LFOs. A summary and discussion of the major results follow in section 6.

## 2. Data and Methodology

### 2.1. Data

[10] This study uses averaged daily data from the National Centers for Environmental Prediction/National Center for Atmospheric Research (NCEP/NCAR) reanalysis [*Kalnay et al.*, 1996]. The data set covers the 53-year-long interval from 1 January 1948 to 31 December 2000. A shorter data set that spans 41 years from 1958 to 1998 was found to yield very similar results [*Koo*, 2001]. The variable analyzed in this study is tropospheric zonal wind in the SH with a horizontal resolution of 2.5 in both latitude and longitude, given on 12 pressure levels: 1000, 925, 850, 700, 600, 500, 400, 300, 250, 200, 150, and 100 hPa.

[11] First, the zonal wind data are zonally averaged. This is justified by the fact that the leading mode of LFV of the SH tropospheric circulation is nearly zonally symmetric owing to the limited role of lower-boundary asymmetries (see section 1). The annual and semiannual cycle are then removed from the daily zonal-mean wind data to define the unfiltered anomalies. The seasonal cycle is estimated by computing the 53-year climatology for each calendar day, followed by a smoothing with a 20-day low-pass filter to remove sampling noise. The results to be shown in section 3 are insensitive to the cutoff frequency of this filter. It is the annual and semiannual components of this filtered cycle [*Van Loon*, 1967] that are removed from the zonal-mean wind data.

[12] *Hartmann and Lo* [1998] noted that the midlatitude zonal jet in the SH exhibits much less pronounced seasonal variation compared with that in the NH. They showed that zonal-flow vacillation in the SH has a similar structure in all seasons and performed their analysis without seasonal stratification.

[13] Following this approach, we analyze data for the entire calendar year, which greatly increases sample size and thus the confidence of PDF estimation. The unfiltered zonal-mean wind data set contains interannual and longer-timescale variability, including a long-term trend. In order to focus on the intraseasonal timescale of the vacillation, as discussed in section 1, we apply a high-pass digital filter with a cutoff at 1 year to the unfiltered anomalies. This high-pass filtered data set is then analyzed carefully in terms of probability density estimation and spectral analysis.

### 2.2. Statistical Methodology

[14] The most elementary way to estimate a PDF is to construct histograms. For example, *Hartmann and Lo* [1998] constructed a one-dimensional histogram for the PC-1 of zonal-mean zonal wind. A shortcoming of histograms is that the overall shape of the PDF is sensitive to the number of bins, and it is difficult to find an optimal way to choose it. Furthermore, it is also known that inhomogeneity, i.e., deviations from Gaussianity, of the PDF can be identified more clearly in a multidimensional space than in one dimension [*Mo and Ghil*, 1988].

[15] In order to overcome these difficulties, we employ a multivariate kernel density estimator [*Silverman*, 1986]. We adopt the adaptive version of the kernel method with the Epanechnikov kernel, as used by *Kimoto and Ghil* [1993a]. In this method the smoothness of final density estimates is controlled by the smoothing parameter  $h$ , whose counterpart in histograms is the number of bins. Unlike histograms, this parameter can be determined objectively using least squares cross-validation (LSCV), which minimizes an estimate of the integrated square error of the PDF [*Silverman*, 1986]. The minimum of the LSCV scores provides the optimal choice for the smoothing parameter. In contrast to the previous studies of univariate density estimations discussed in section 1, we estimate the PDF in a two-dimensional (2-D) phase space, spanned by the two leading EOFs of zonal-mean flow.

[16] In order to examine the temporal behavior of the mode that represents zonal-flow vacillation, we adopt two complementary methods of spectral analysis: the multitaper method (MTM) and singular-spectrum analysis (SSA). MTM [*Thomson*, 1982, 1990; *Mann and Lees*, 1996]

provides better and more reliable spectral estimates than the classic Blackman-Tukey correlogram method by using a small set of optimal windows (tapers) that objectively minimize power leakage and reduce estimate uncertainties. We assess statistical significance against a red-noise null hypothesis by fitting a first-order autoregressive (AR(1)) process to the time series, according to the method of *Mann and Lees* [1996].

[17] SSA [*Broomhead and King*, 1986; *Fraedrich*, 1986; *Vautard and Ghil*, 1989; *Vautard et al.*, 1992] is a form of principal component analysis in the time domain and describes the variability of the time series in terms of its autocovariance structure. Its data-adaptive nature gives SSA an advantage over other spectral methods in detecting anharmonic oscillations of possibly nonlinear origin. An oscillatory component is represented in SSA by a single pair of temporal EOFs, rather than by multiple spectral peaks.

[18] We conduct significance tests of any oscillatory pairs found against a red-noise null hypothesis using the Monte Carlo method of *Allen and Smith* [1996]. An ensemble of 100 red-noise surrogate time series are generated, each with the same length and the same lag-0 and lag-1 autocorrelation as the time series to be tested. The data and AR(1) noise realizations are then projected onto the EOFs of the data covariance matrix.

### 3. Probability Density Estimation

[19] We apply the kernel density estimator to the high-pass filtered data, as described in section 2. EOF analysis is performed, prior to PDF estimation, by diagonalizing the covariance matrix of the zonal-mean flow anomalies.

[20] Figure 1 shows the two leading EOFs, which account for 28.8% and 15.4% of total variance, respectively. Both modes have approximately an equivalent-barotropic vertical structure. Consistent with previous SH observations [*Yoden et al.*, 1987; *Kidson*, 1988; *Hartmann and Lo*, 1998], the first EOF exhibits dipolar variability with opposite anomaly centers near 40°S and 60°S. The node is located near 50°S, which corresponds roughly to the climatological position of the midlatitude, eddy-driven [*Hartmann and Lo*, 1998] zonal jet. Therefore EOF-1 represents the meridional displacement of the zonal jet from its climatological mean position. The second EOF shows a similar structure to the first EOF, but its two main variability centers are shifted further poleward.

#### 3.1. Choice of Reduced Phase Space

[21] We first consider data scatter in phase space and its implications for PDF estimation. Data scatter in terms of “signal” and “noise” is illustrated in Figure 2, following *Kimoto and Ghil* [1993a]. In Figures 2a and 2b the abscissa denotes the signal component defined by

$$\|\mathbf{x}\|_S \equiv \left( \sum_{i=1}^s c_i^2 \right)^{1/2} \quad (1)$$

and the ordinate indicates the noise component defined by

$$\|\mathbf{x}\|_N \equiv \left( \sum_{i=s+1}^{10} c_i^2 \right)^{1/2}; \quad (2)$$

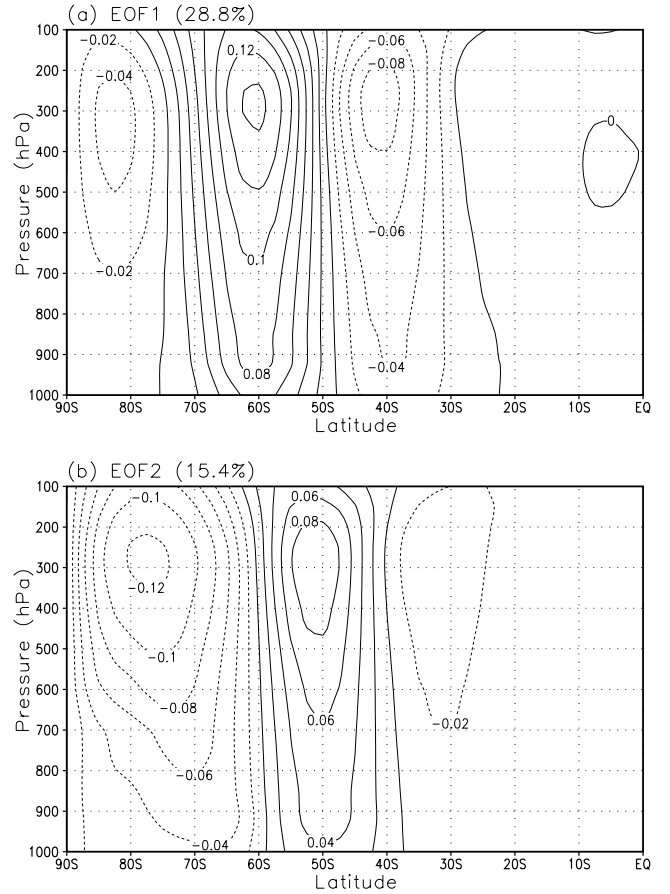


**Figure 1.** The two leading EOFs of the zonal-mean flow anomalies; see text for details.

here  $c_i$  is the  $i$ th PC, while  $s = 1$  in Figure 2a and  $s = 2$  in Figure 2b. The diagonal line indicates a signal-to-noise ratio of 1. We have chosen in Figure 2 to truncate the “noise” at 10 leading EOFs. These 10 EOFs capture 84.7% of total variance, and the results in the figure are found to be insensitive to increases in this number.

[22] If we take EOF-1 as the sole physical signal of zonal-mean flow variability, the majority of the data points fall into the upper triangle of Figure 2a, where the signal-to-noise ratio is  $\sim 1$ . On the other hand, if we let the two leading EOFs be the physical signal, as shown in Figure 2b, the signal-to-noise ratio becomes substantially enhanced. Furthermore, many data points which previously lay near the climatological mean state are now away from the origin. This result implies that if a PDF or histogram is computed using only PC-1, as given by *Akahori and Yoden* [1997] or *Hartmann and Lo* [1998], a large fraction of the data points will fall near the origin; hence any bimodality that might be present in the data could be obscured by noise. In order to avoid this situation, we proceed with PDF estimation in a 2-D subspace spanned by the two leading EOFs.

#### 3.2. PDF Estimates for the Entire Data Set

[23] The smoothness of the PDF is determined objectively using LSCV, whose scores are plotted as a function of the smoothing parameter  $h$  in Figure 3. The estimated score has a minimum value at  $h = 0.4$ , although the curve has a

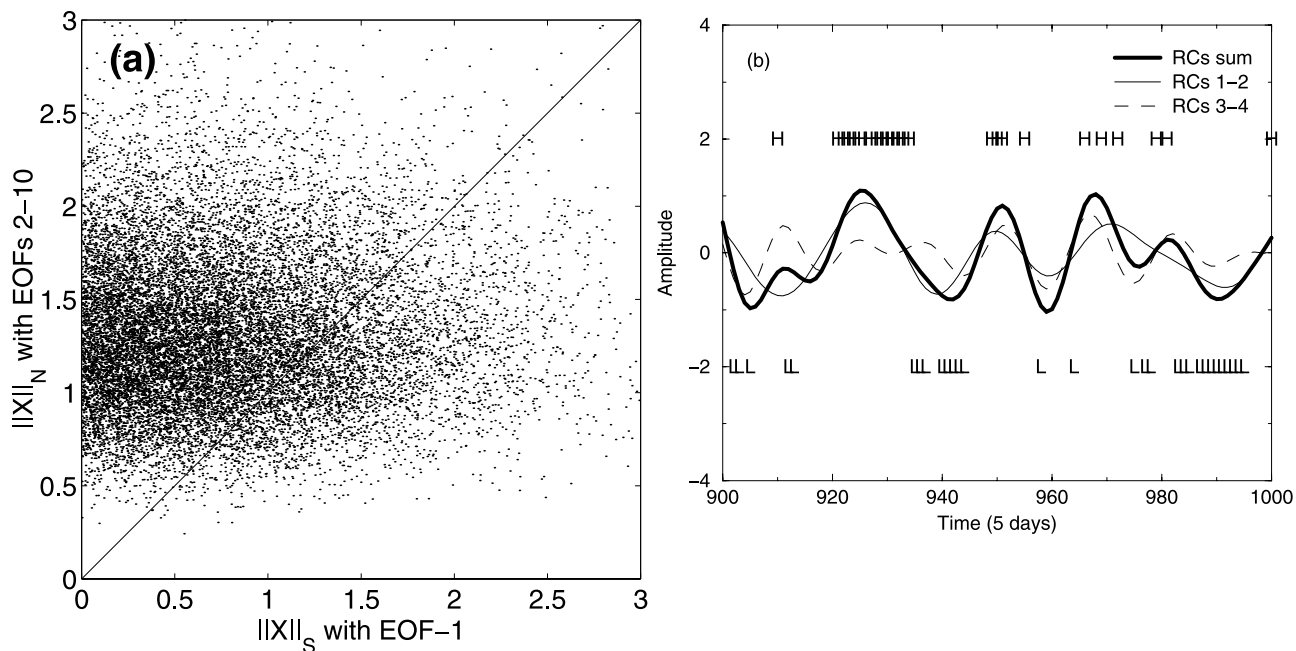


**Figure 2.** Data scatter in terms of leading EOFs. (a) Abscissa is the root-mean square (RMS) magnitude of anomalies computed using only PC-1, while the ordinate is the RMS magnitude of anomalies using PC-2 through PC-10. (b) Abscissa is the RMS magnitude of anomalies computed with PC-1 and PC-2, while the ordinate is the RMS magnitude of anomalies with PC-3 through PC-10.

fairly broad bottom, with almost equal values at  $h = 0.3$  and  $0.4$ , as is often the case in LSCV.

[24] The PDF in our 2-D phase space is now estimated using the smoothing parameter  $h = 0.4$  and is shown in Figure 4a. A similar but slightly less smooth PDF is obtained with  $h = 0.3$  (not shown). The 2-D PDF has an overall elliptical shape. In the central region a PDF peak and a shoulder attached to it are located slightly away from the center. Despite the large sample size of 18,395 days, the PDF shows deviations from a theoretical bivariate Gaussian.

[25] We quantify the distinction between the visual deviations from Gaussianity in Figure 4a and sampling variability by conducting Monte Carlo simulations. One hundred sets of red-noise time series that have the same length as the original PC time series are generated using a 2-D AR(1) model described in Appendix A. The model parameters are listed in Table 1.

[26] One hundred random PDFs are computed from these synthetic PC time series using the same kernel method with the same smoothing parameter  $h = 0.4$  as in Figure 4a. The percentage of random PDFs so generated that fall short of the PDF values shown in Figure 4a is plotted in Figure 4b, with regions containing values above 95 shaded. Both the peak and the shoulder in Figure 4a are significant at the 95% confidence level. In addition to these regions, a ridge in the first quadrant that extends from the point  $(0.6, 0.5)$  to the point  $(1.0, 1.0)$  is significant at the 95% confidence level.

[27] In addition to this local test of statistical significance of the PDF we perform a global significance test due to Hsu and Zwiers [2001]. This test determines whether the significant local departures from a Gaussian PDF contribute a globally significant amount of probability. To do so, one integrates an estimated PDF over the areas that were identified as significant in the local test and then ranks this

statistic, the so-called IPDF, against the probabilities obtained by integrating the synthetic PDFs over their respective areas of local significance. The global significance test applied to our data indicates that 96% of the synthetic PDFs have an integrated probability that is lower than the corresponding IPDF of the original PC data. We thus conclude that the three major regions shaded in Figure 4b are highly significant locally as well as globally.

### 3.3. PDF Estimate of Quasi-Stationary Data

[28] Various methods for ascertaining the existence of multiple flow regimes in atmospheric data sets have recently

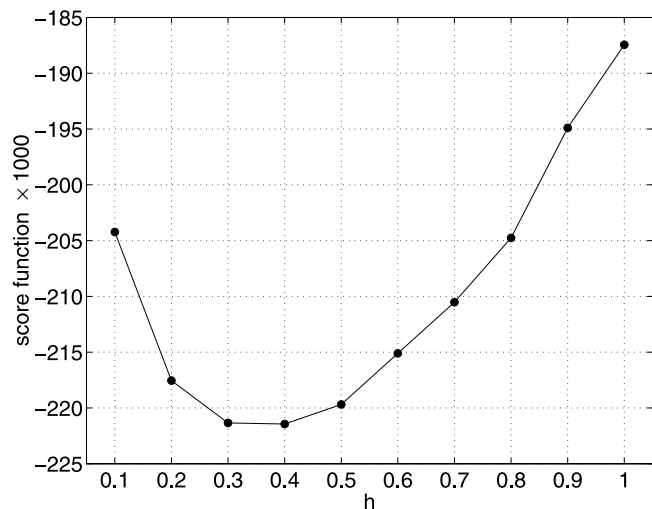


**Figure 3.** Least squares cross validation (LSCV) scores as a function of the smoothing parameter  $h$ .

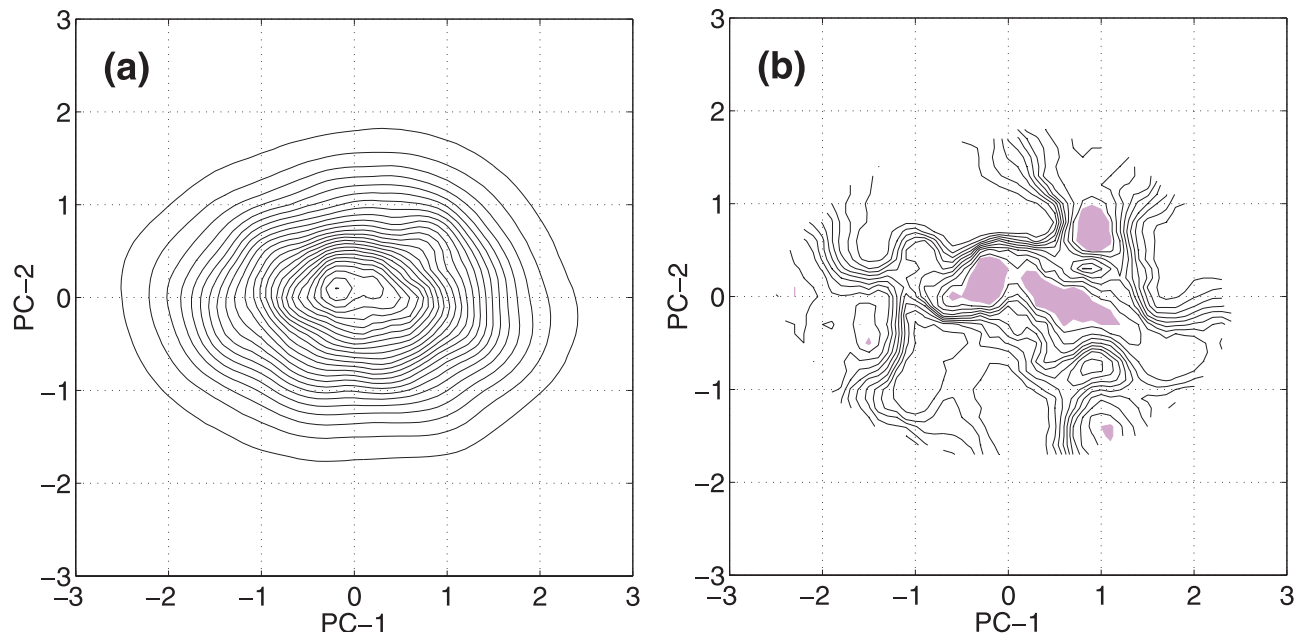


**Figure 4.** Estimated PDF of the zonal-mean flow anomalies. (a) Two-dimensional PDF in a plane spanned by EOF-1 and EOF-2, with a smoothing parameter of  $h = 0.4$ . Axes are scaled by the standard deviation of PC-1; contours are drawn from 0.01 with interval 0.01. (b) Number, out of 100, of random PDFs that fall short of the PDF values shown in Figure 4a. Contours are drawn from 10 to 90 with interval 10; the regions with values larger than 95 are shaded.

been reviewed by *Ghil and Robertson* [2002]. In order to corroborate the evidence of recurrent flow regimes identified in Figure 4, we consider a quasi-stationary (QS) data subset. A QS subset can be constructed by selecting samples that are quasi-stationary under a given measure of similarity.

[29] Two different measures, pattern correlation [*Mo and Ghil*, 1988; *Kimoto and Ghil*, 1993a] and Euclidean distance [*Vautard et al.*, 1988; *Koo*, 2001], have been widely used so far. Although these two measures are not entirely independent, they possess complementary characteristics. Pattern correlation is defined as the cosine of angular distance and neglects the amplitude of the anomaly, while Euclidean distance is a Cartesian measure and does not distinguish between changes in pattern and changes in amplitude. Owing to this difference a QS subset based on pattern correlation tends to favor maps with large-amplitude anomalies, while a QS subset based on Euclidean distance has a bias toward small-amplitude anomaly maps that have less meteorological significance.

[30] To illustrate this point, consider two line segments in a 2-D plane that have the same length, but one is located close to the origin and the other one lies far from it. The angular distance between the end points of the line segment that lies close to the origin is much larger than the other one, when viewed from the origin. Thus subsampling based on small angular distance has a bias toward maps with a large-amplitude anomaly. On the other hand, subsampling based on small Euclidean distance has the opposite bias toward maps with small-amplitude anomalies, regardless of their patterns. These small-anomaly samples may be less interesting, since meteorological experience attaches larger physical significance to the pattern of an anomaly relative to its magnitude [*Kimoto and Ghil*, 1993b].

[31] For these reasons, we construct a QS data subset using both complementary measures of similarity. First, we compute the Euclidean and angular distance between two samples one day apart in 10-D phase space. The relationship between these two measures is shown in Figure 5 as a scatterplot. The two are relatively well correlated: their correlation coefficient is 0.6244. Our QS subset is defined by collecting the points that fall into the lower left corner, below the linear regression line (solid line) and to the left of the mean value of the Euclidean distance (dashed line). These points exhibit quasi-stationarity in terms of both distance measures. The resulting QS subset consists of 6066 maps, which constitute 33.0% of the original data set.

[32] The QS subset is then projected onto the two leading EOFs of the original data that appear in Figure 1. The PDF of the QS subset is estimated using a smoothing parameter of  $h = 0.6$ , as chosen by the LSCV for this subset, and is shown in Figure 6a. The PDF exhibits pronounced bimodality, with two distinct peaks situated far apart along the PC-1 axis. A narrow shoulder is attached to the PDF peak that lies near the positive PC-1 axis. This shoulder runs roughly parallel to the PC-2 axis and it corresponds to the significant ridge identified in Figure 4.

[33] As in section 3.2, we estimate the statistical significance of the two PDF peaks in Figure 6a. First, 100 sets of synthetic PC time series are generated using an AR(1) model in 10 dimensions (10-D), which is a 10-D extension

**Table 1.** Parameter Estimates for the Linear Stochastic Model

| $E(Z_i)$ | $\Phi$ |         | $\Sigma$ |        |
|----------|--------|---------|----------|--------|
| 0.0000   | 0.9425 | -0.0611 | 0.1097   | 0.0139 |
| 0.0000   | 0.0157 | 0.8789  | 0.0139   | 0.1215 |

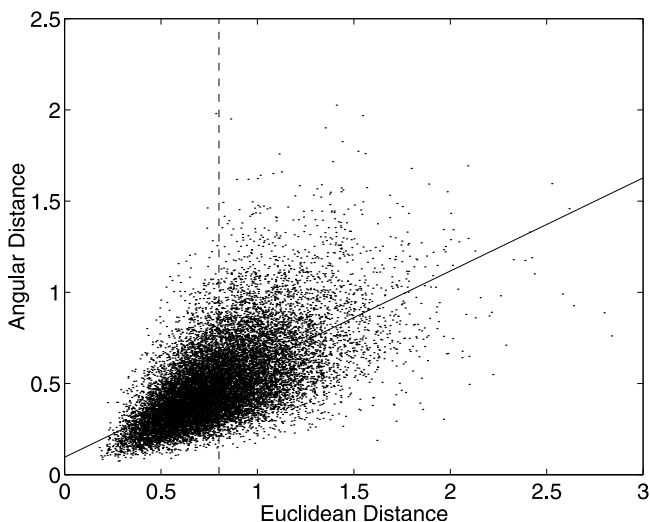


**Figure 5.** Data scatter in terms of two distance measures. The sloping solid line indicates a least squares linear fit; the vertical dashed line denotes the mean value of the Euclidean distance.

of the linear stochastic model described in Appendix A. All the synthetic time series have the same length as the original PC time series. These synthetic time series are then subject to the same QS sampling and the same PDF estimation. The percentage of the resulting random PDFs that fall short of the QS PDF values shown in Figure 6a is plotted in Figure 6b, with regions containing values above 95 shaded. Both peaks in Figure 6a are significant at the 95% confidence level, and the two regions of high significance are well separated by a narrow neck in the shading.

[34] Owing to our subsampling procedures the synthetic QS subsets do not have the same length as the original QS

subset. The median length of the synthetic QS subsets is 5630, which is  $\sim 7\%$  shorter than the original QS subset. We have carefully checked whether our QS procedures introduce any bias into the subsequent PDF estimations. First, before any QS subsampling, the scatterplots of the two distance measures for the 10-D synthetic data are visually checked. They are found to be nearly identical to Figure 5. Next, we conducted LSCV for each QS subset of the synthetic data. The optimal value of the smoothing parameter is the same for all synthetic QS subsets and equals the one for the original QS subset.

[35] In addition to Figure 6b, where  $h = 0.6$  is used for both the original and synthetic QS subsets, we repeated the same analysis with the smaller value of  $h = 0.5$  for the synthetic QS subsets, while keeping  $h = 0.6$  for the original QS subset. This intentional bias applies less smoothing to the synthetic QS subsets and thus enhances their PDF peaks preferentially; in spite of this, the result (not shown) remains very similar to Figure 6b.

[36] We also conduct the global significance test of *Hsu and Zwiers* [2001], as in section 3.2. The global significance test applied to the QS data set indicates that none of the synthetic PDFs have an integrated probability that is greater than the corresponding IPDF of the original QS data. Thus the two PDF peaks in Figure 6a are highly significant, locally as well as globally.

[37] The PDF of the QS subset provides additional evidence of multiple flow regimes that correspond to recurrent and quasi-stationary states of the zonal-mean flow. The difference between the PDFs shown in Figure 4a and Figure 6a demonstrates that transient noise near the time mean state can obscure inherent bimodality present in the full data set.

### 3.4. Regime Composites

[38] Our PDF estimations shown in Figures 4 and 6 strongly suggest the existence of two or three recurrent

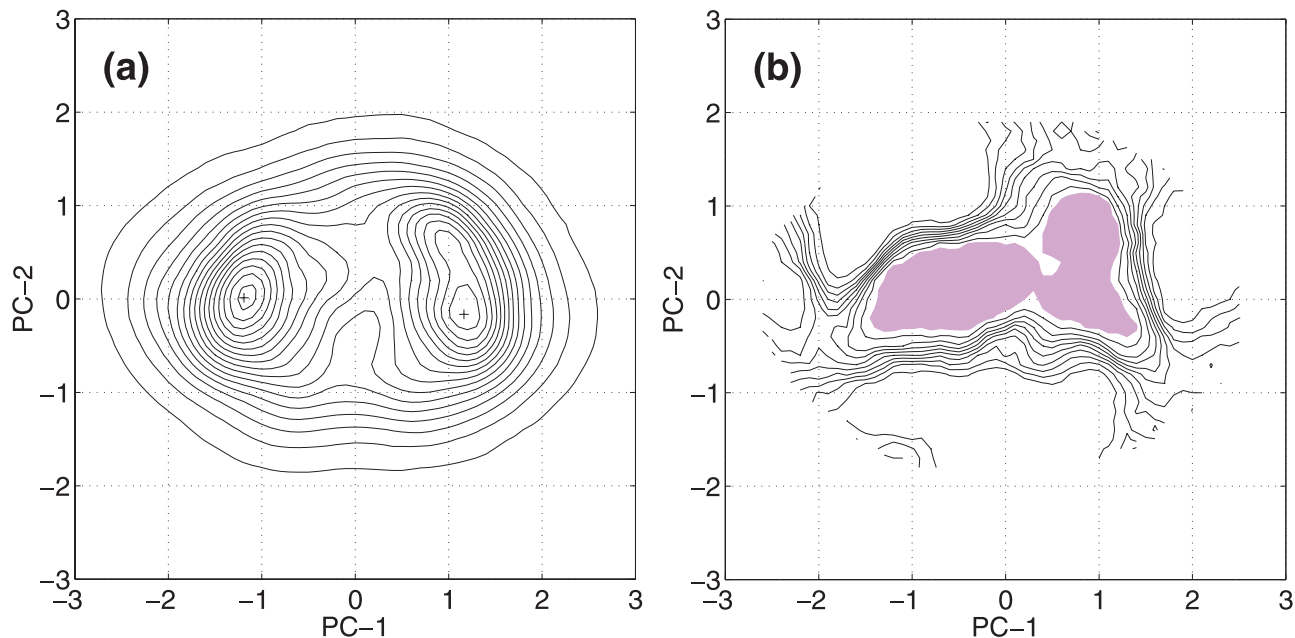


**Figure 6.** Same as Figure 4 but for the QS subset with a smoothing parameter of  $h = 0.6$ . The plus symbol in Figure 4a denotes the two regime centroids (see text for details).

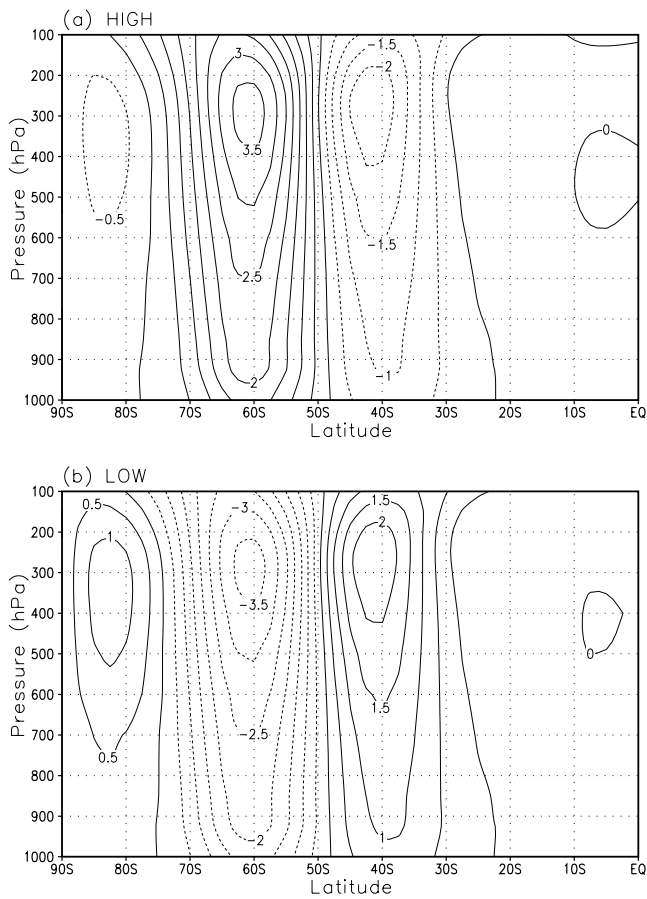


**Figure 7.** Composites of zonal-mean flow anomalies for the (a) high-latitude and (b) low-latitude regime days. Contour interval is  $0.5 \text{ m s}^{-1}$ ; solid contours are positive and dashed ones are negative.

and quasi-stationary regimes. We investigate the physical space picture associated with the two major regimes that are located along the PC-1 axis. First, the two centroids of recurrent and quasi-stationary regimes are defined by the centers of the two PDF peaks in Figure 6a. These regime centroids are precisely located by using the bump-hunting algorithm of *Fukunaga and Hostetler* [1975] and are denoted by the plus symbol in Figure 6a. We then collect all the points in the full data set that fall within the radius of 1.0 Euclidean distance from these centroids in the 2-D phase space spanned by the two leading EOFs. A total of 5508 and 5168 days out of 18,395 days are assigned to the regimes that are located on the positive and negative PC-1 axis, respectively. Finally, anomaly fields in physical space that corresponds to these selected regime days are composited.

[39] The two flow composites so obtained are plotted in Figure 7. Two distinctively different anomalous zonal-jet states are identified. These two regimes represent the two extreme phases of zonal-flow vacillation, with the jet displaced either poleward (high-latitude regime) or equatorward (low-latitude regime) from its time-mean position.

[40] Figure 8 shows eddy momentum flux anomalies composited with respect to the high- and low-latitude regimes. Two opposite states, relative to the annual cycle, of eddies are clearly visible. During the high-latitude

regime, negative eddy momentum flux anomalies centered near  $50^{\circ}\text{S}$  act to enhance the poleward transport of eastward momentum by eddies. Positive eddy momentum flux anomalies for the low-latitude regime weaken poleward transport of eastward momentum by the eddies. These eddy momentum flux anomalies lead to positive anomalies of momentum flux convergence near  $60^{\circ}\text{S}$  and  $40^{\circ}\text{S}$  for the high- and low-latitude regime, respectively.

[41] Owing to the stationary eddies in the SH being relatively weak (see *Newton* [1972] and discussion in section 1 here), eddy momentum forcing of the mean zonal flow comes mostly from transient eddies (not shown). According to Figure 8, this eddy forcing tends to maintain the zonal-mean flow anomalies shown in Figure 7 against surface friction, a result that agrees with previous observational studies [*Karoly*, 1990; *Hartmann and Lo*, 1998].

[42] Transformed Eulerian mean diagnostics [*Andrews and McIntyre*, 1976; *Edmon et al.*, 1980] provide another way to examine wave-mean-flow interaction. In this framework, zonal-mean flow forcing by eddy fluxes of heat and momentum is expressed by the divergence of the Eliassen-Palm flux. *Yoden et al.* [1987] examined the Eliassen-Palm flux and its divergence for their single- and double-jet regimes and found that larger wave drag maintains a weaker polar night jet in the single-jet regime. Using the same diagnostics, *Koo* [2001] also showed that total eddy forcing

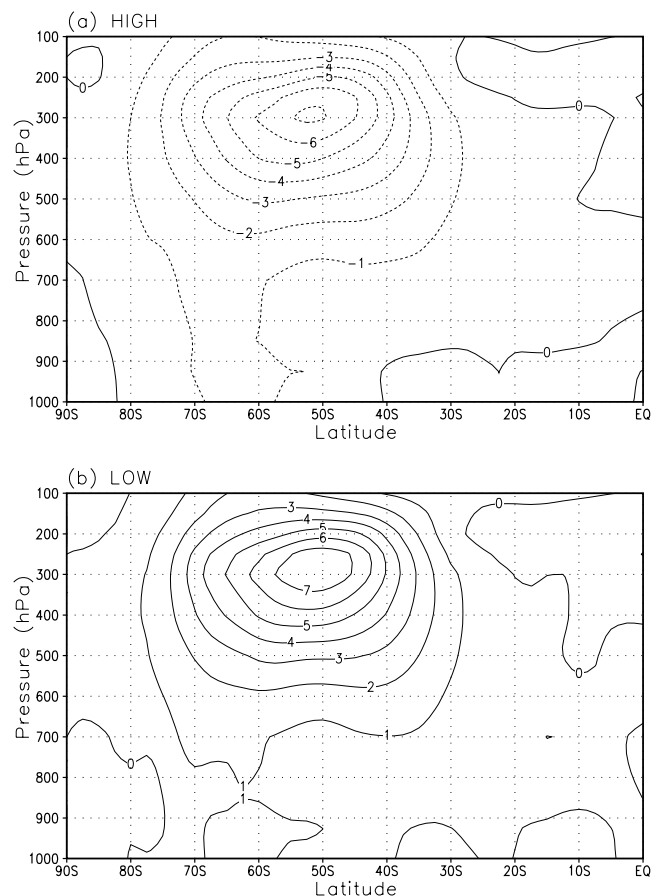


**Figure 8.** Same as Figure 7 but for eddy momentum flux. Contour intervals are  $1.0 \text{ m}^2 \text{ s}^{-2}$ .

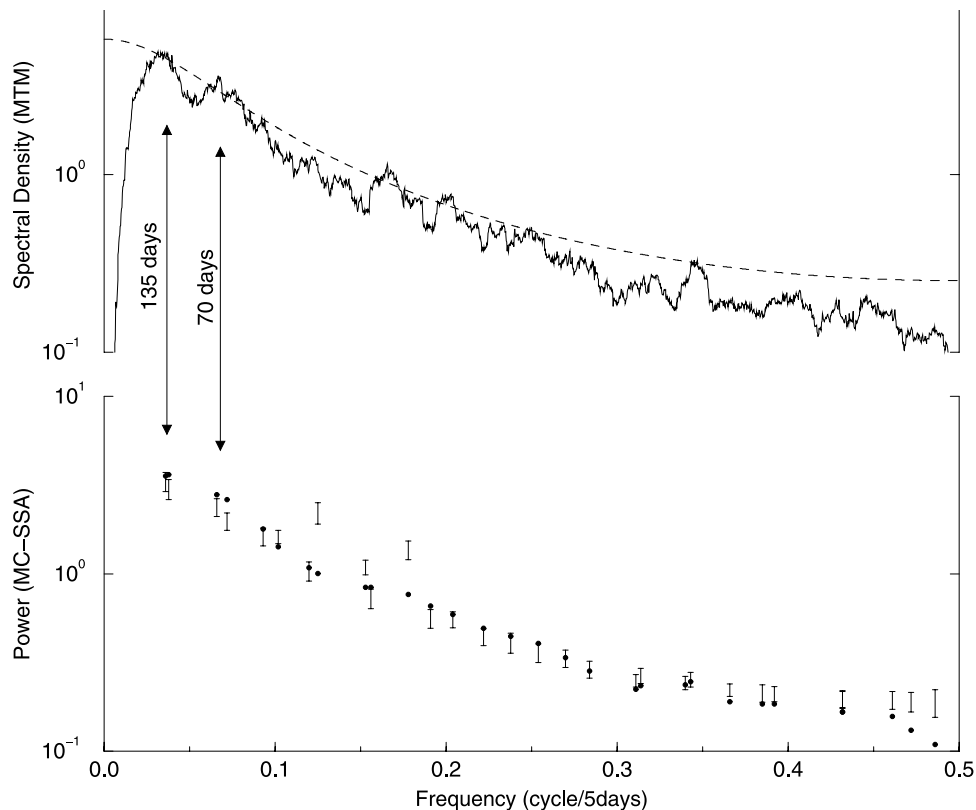


**Figure 9.** Spectral analysis of the zonal-mean flow's PC-1. (top) A spectrum estimated by the multitaper method (MTM) and (bottom) a spectrum estimated by Monte Carlo singular spectrum analysis (MC-SSA). In the MTM spectrum, solid lines are spectral estimates, while dashed lines represent a 99% confidence level with respect to a red-noise null hypothesis. In the MC-SSA spectrum, the confidence intervals are bounded by the 5% and 95% percentiles of Monte Carlo simulations of a red-noise process.

acts to maintain the high- and low-latitude regimes against surface friction.

#### 4. Spectral Analysis

[43] In this section we critically examine any evidence of low-frequency oscillations (LFOs) that are associated with atmospheric zonal-flow vacillation. To do so, two advanced spectral analysis techniques, MTM and SSA (see section 2.2 and *Ghil et al.* [2002]), are applied to the leading PC of the zonal-mean flow anomalies that are high-pass filtered at 1 year.

[44] Similar results were obtained from a multichannel SSA analysis of the two leading PCs. The spatiotemporal patterns of the oscillatory modes were found to be dominated by the leading PC (not shown). We therefore restrict for simplicity the presentation of the results to those obtained by analyzing PC-1.

[45] As a first step, 5-day nonoverlapping box-car averages of the PC-1 time series are taken in order to focus on intraseasonal timescales. We then apply both MTM and SSA to the resulting time series. In MTM, 39 tapers are used; these yield a half-bandwidth spectral resolution of 0.013 cycle/(5 days). In SSA, we chose a lag window of  $M = 30$  to target intraseasonal oscillatory modes; this allows a window width of 150 days that corresponds very approximately to a spectral resolution of  $1/M = 0.033$  cycle/(5 days).

[46] The resulting spectra are shown in Figure 9. Both independent estimation algorithms identify two common oscillatory components with peaks near 135 and 70 days. Both oscillatory components are statistically significant at the 99% confidence level by MTM [*Mann and Lees*, 1996] and at the 95% level using SSA. MTM identifies two additional peaks near 30 and 25 days, which are statistically significant at the 99% level. These oscillatory components are not found to be highly significant by SSA for the full 53-year data set on which we have based most of our analyses (see section 2.1); the 30-day peak is significant, though, at the 95% level when applying SSA to the shorter data set that covers the 41 years from 1958 to 1998 [*Koo*, 2001].

[47] We have also examined oscillatory components in the unfiltered PC-1 time series (not shown). MTM finds the same three oscillatory components as in the results of the high-pass filtered data set above. The 70- and 30-day oscillations are significant at the 99% level, and the 135-day oscillation is significant at the 95% level.

[48] The fact that the 70-day oscillation's period is close to one half of the 135-day period suggests that it might be a harmonic of the 135-day oscillation. We investigated whether the two oscillations are phase-locked, using a method similar to that of *Plaut and Vautard* [1994], *Dettinger and Ghil* [1998], and *Moron et al.* [1998]. Little evidence was found to support this possibility (not shown).

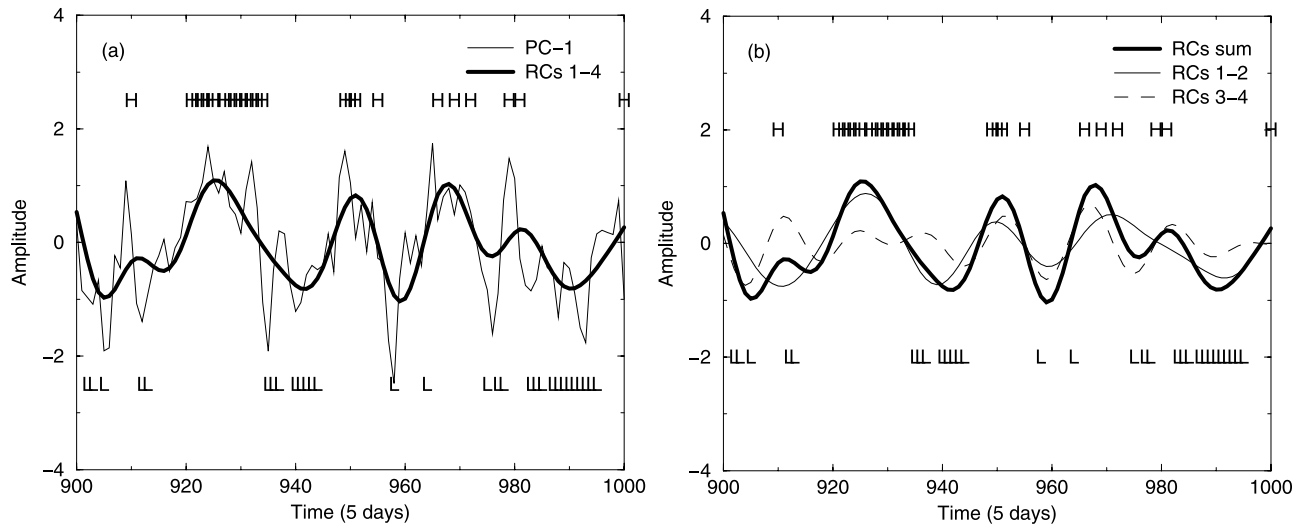


**Figure 10.** Comparison between regime episodes and oscillation phases for a sample interval of 18 August 1961 to 31 December 1962. (a) 5-day mean PC-1 (light solid line) and its reconstructed components (RCs 1–4; heavy solid line) using a 150-day SSA window. Regime chronology is also displayed using the symbols H and L to indicate the high- and low-latitude events, respectively. (b) Decomposition of the reconstruction of Figure 10a, shown here also as heavy solid, into two separate RC pairs. Light solid lines are RCs 1–2 ( $T=135$  days), and dashed lines are RCs 3–4 ( $T=70$  days), where  $T$  refers to the approximate period of oscillation.

[49] We now inspect the two oscillatory components within a sample period of 505 days, between 18 August 1961 and 31 December 1962. Figure 10 shows the two pairs of reconstructed components (RCs), 1–2 and 3–4, which represent the two SSA oscillatory components found in Figure 9, along with the box-car filtered PC-1 time series. These RC pairs are narrowband-filtered versions of the time series, where the filters are derived data-adaptively from the time series itself in order to maximize the variance captured [Ghil and Vautard, 1991; Vautard et al., 1992]. The two RC pairs account for 28.0% and 21.0% of the variance of the PC-1 time series, respectively. Their sum (heavy solid line in Figure 10a) traces well, in general, the excursions of the PC-1 time series (light solid line in Figure 10a).

[50] As part of the work discussed in section 3, a so-called regime chronology was computed on the basis of daily data. In order to compare the daily regime chronology with the time evolution of the 5-day filtered PC-1 and its RCs, we use the following ad hoc procedure. First, values of +1 and –1 are assigned to the days classified as belonging to the high-latitude and low-latitude regimes, respectively. The days that are not classified into either of the regimes are assigned a value of zero. We then take 5-day nonoverlapping box-car averages of the resulting time series. If a 5-day average value is  $\geq 0.6$ , the corresponding 5-day time span is considered to belong to the high-latitude regime. Similarly, if this value is  $\leq -0.6$ , the corresponding time span is assigned to the low-latitude regime.

[51] In this way, the daily regime chronology is converted to the 5-daymean chronology that is shown in Figure 10 by using the symbols H and L. Despite the somewhat ad hoc nature of the procedure, both regimes in the chronology tend to agree rather well with extrema in the 5-day mean PC-1 time series. Furthermore, the occurrence of either regime often coincides with extrema in one of the individual

RC pairs. This correspondence is further investigated in section 5.

## 5. Multiple Flow Regimes and Low-Frequency Oscillations

[52] Good visual correspondence between the regime chronology and the time evolution of the LFOs in Figure 10 suggests complementarity between these two distinct descriptions of midlatitude LFV. This possibility was proposed by Ghil and Childress [1987, chapter 6] and by Kimoto and Ghil [1993b]. Plaut and Vautard [1994] examined it in detail for the NH’s Atlantic-European region.

[53] To further explore the relationship between each LFO and regime events, the evolution of zonal-flow regime events in a planes panned by each RC pair and its tendency RC is plotted in Figure 11, following Plaut and Vautard [1994]. The high-latitude (heavy grey segments) and low-latitude (light black segments) regimes correspond quite well to the two opposite phases of both the 135-day and the 70-day oscillations. The results shown in Figure 10 and Figure 11 suggest that zonal-mean flow regimes are associated with the slow phases of the 135-day and 70-day oscillatory modes in the PC-1 time series.

[54] The general correspondence between the zonal-flow regimes and the slow phases of the LFOs implies that transitions between the high- and low-latitude regimes may not be entirely driven by random perturbations. This provides hope for improved long-range forecasts of zonal-mean flow regimes, since oscillations are, by nature, more predictable than episodic regime events. Better predictions of zonal-flow regimes would benefit medium- to long-range weather forecasts owing to the close links between variations in the upper-level jet’s position and intensity, on the one hand, and changes in synoptic-scale weather patterns,

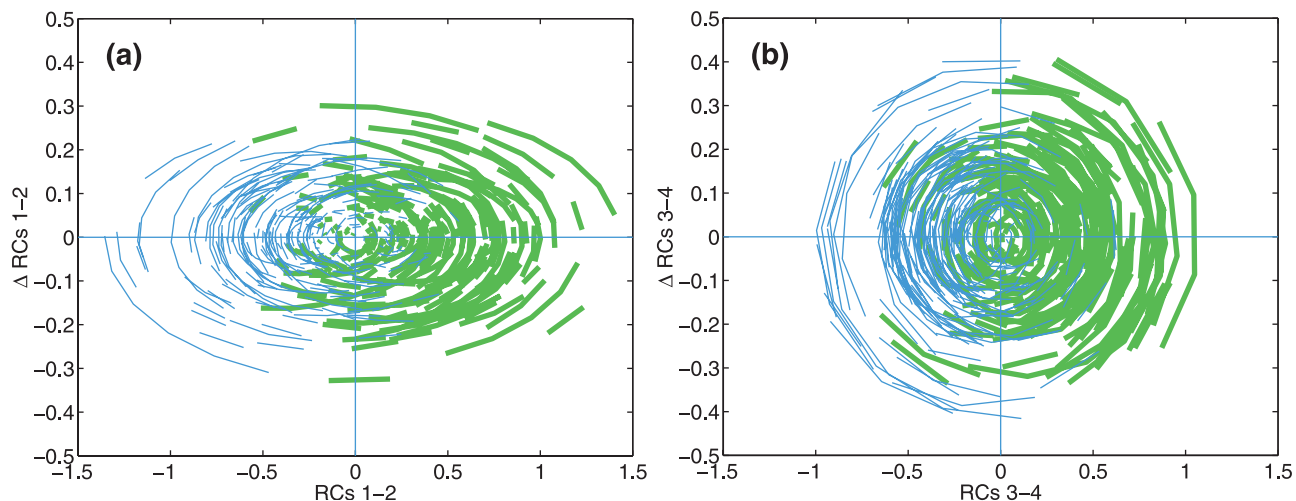


**Figure 11.** Regime events projected onto the plane spanned by the RCs and their tendency: (a) 135-day and (b) 70-day oscillations. The high-latitude regime events are denoted by heavy grey segments, while the low-latitude regime events are indicated by light black segments. The tendencies  $\Delta RC$  are defined by the centered finite difference between two RC values 2 days apart, divided by the time elapsed.

on the other. For example, using the multidecadal simulations of a general circulation model, *Watterson* [2000] showed that the vacillation is closely related to low-frequency variations of many meteorological variables, such as temperature, surface pressure, cloud cover, and rainfall.

[55] We illustrate next how the phase information of the 70-day oscillation could be used as a predictor for the two extreme phases of zonal-flow vacillation. Similar results were obtained using the 135-day oscillation (not shown). It is the extreme events with very large amplitudes in zonal-mean flow anomalies that have the greatest meteorological impact. We focus, therefore, on high- and low-latitude states that have normalized PC-1 amplitude  $>1.0$ , rather than on the regimes as a whole. Similar but slightly less striking results are obtained when the high- and low-latitude regimes are considered (not shown).

[56] We define a phase category of an LFO as follows. The LFO is represented by the scalar sum  $Y(t_i) = Y_i$  of an RC pair; its instantaneous phase  $\phi_i$  is defined as the angle between the instantaneous vector  $(Y_i, \dot{Y}_i)$  and the vector  $(0, 1)$ , where  $\dot{Y}_i$  is the local tendency of  $Y_i$ . Each phase  $\phi_i$  is then assigned to one of eight phase categories. These categories are constructed by dividing the interval  $(0, 2\pi)$  into eight equally populated segments so that each phase category contains the same number of  $\phi_i$ .

[57] Figure 12 shows the conditional probability of the zonal-mean flow states occurring at lead times of 0 to 200 days when the phase category of the 70-day oscillation is known on day 0. Conditional probabilities are plotted for phase categories 3 and 7 when predicting the high- and low-latitude states, respectively. Given the condition that the current phase of the 70-day oscillation is in category 3, the probability of occurrence of the high-latitude state 65 days later is  $\sim 57\%$  higher than the unconditional climatological forecast, and it is  $\sim 91\%$  higher than the persistence forecast.

[58] Conditional probabilities for the low-latitude state are even higher than those for the high-latitude state at the same lead time. For example, when the current phase of the 70-day oscillation is in category 7, the probability of occur-

rence of the low-latitude state 70 days later is  $\sim 84\%$  higher than the unconditional climatological forecast, and it is  $\sim 120\%$  higher than the persistence forecast.

[59] We have repeated the above analysis with the 135-day oscillatory component. The results (not shown) are actually somewhat better than those obtained for the 70-day component (Figure 12). At 70-day lead, for example, the conditional probabilities of high- and low-latitude states are  $\sim 85\%$  and  $105\%$  higher than the respective unconditional probabilities.

## 6. Concluding Remarks

[60] We have examined the evidence for multiple zonal-mean flow regimes in Southern Hemisphere (SH) observations. A kernel density estimator was applied to the 53-year-long daily NCEP/NCAR reanalysis data set in order to compute the probability density function (PDF) of the zonal-mean zonal flow. Anomalies of the zonal-mean flow were high-pass filtered at 1 year to focus on intraseasonal variability.

[61] In the reduced phase space spanned by the two leading EOFs the PDF deviates significantly from a bivariate Gaussian, despite the large sample size (Figure 4a). The deviations include a PDF peak, a shoulder attached to it, and a separate PDF ridge. All three features in the PDF are found to be significant at the 95% confidence level against a red-noise null hypothesis (Figure 4b).

[62] A data subset that represents quasi-stationary (QS) zonal-jet states exhibits two pronounced PDF peaks that are far away from the climatological mean state and a narrow shoulder attached to one of the two peaks (Figure 6a). Compared with the PDF of the full data set (Figure 4a), this pronounced bimodality in the QS subset (Figure 6a) demonstrates that transient noise near the time-mean state obscures the inherent bimodality present in the original data.

[63] Our estimated PDFs (Figures 4 and 6) provide strong evidence for multiple regimes in the SH observations' zonal-mean flow. As discussed in section 1, no conclusive evi-

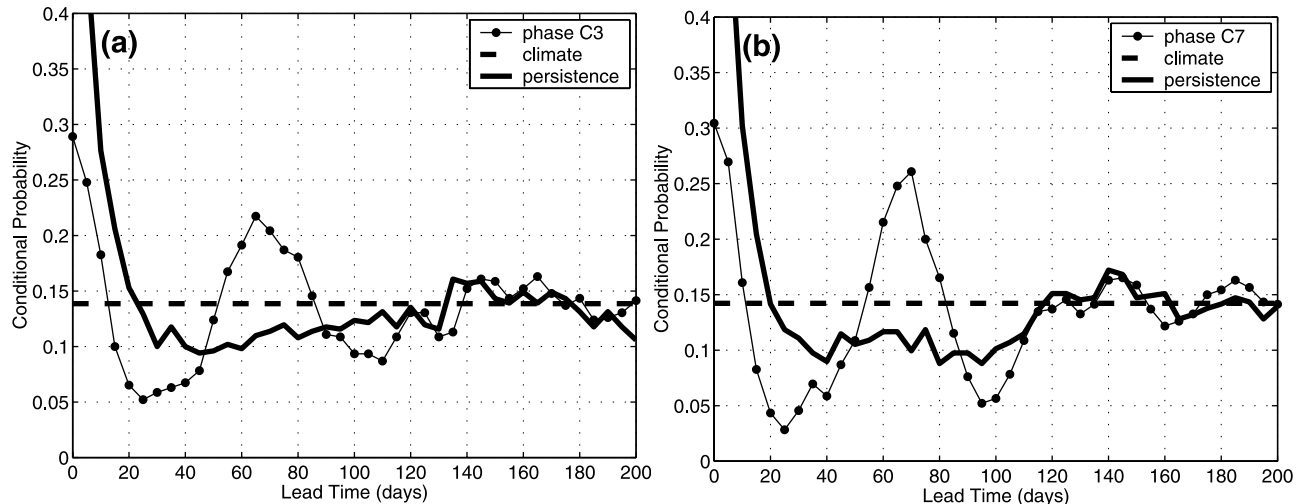


**Figure 12.** Probability of occurrence of (a) high-latitude and (b) low-latitude states, given the phase category of the 70-day oscillation. Heavy horizontal dashed lines indicate climatological probability, and heavy solid curves denote persistence forecasts. Light solid curves with filled circles indicate predictions based on phase information of the 70-day oscillation.

dence concerning this issue was found in previous studies. The major difference between those studies and the present results resides in our use of bivariate density estimators, while previous studies only applied univariate estimators. The analysis of the signal-to-noise ratio (Figure 2) demonstrates the necessity of describing the signal in a reduced phase space having dimension higher than one. We have found that a PDF estimated using PC-1 only does not yield strong evidence of either bimodality or multiple regimes (not shown).

[64] Composites of the two major regimes describe the two opposite phases of zonal-flow vacillation (Figure 7): the jet is displaced either poleward (high-latitude regime) or equatorward (low-latitude regime) from its time mean position. The latitudinal shift of the zonal jet's maximum entails other changes in its profile as well. In fact, when the subtropical jet is strong, for example during the SH winter, zonal-flow vacillation describes the changes in the velocity profile of the midlatitude jet, with a broader or narrower maximum, as well as the changes in its intensity.

[65] Composites of eddy momentum flux for the high- and low-latitude regime days (Figure 8) indicate that the two zonal-flow regimes are maintained by transient-eddy forcing against surface friction. This diagnostic result is consistent with the findings of previous observational studies [Yoden *et al.*, 1987; Karoly, 1990; Hartmann and Lo, 1998] and of our own modeling studies [Koo, 2001; Koo and Ghil, 2002].

[66] Two advanced spectral analysis techniques, MTM and SSA, have been applied to the 53-year-long PC-1 time series of the zonal-mean flow data from the NCEP/NCAR reanalysis. Both MTM and SSA spectra exhibit two common oscillatory modes, with peaks near 135 and 70 days. Both peaks are statistically significant at the 99% confidence level using MTM and at the 95% level according to SSA (Figure 9). The 70-day peak is reminiscent of the 70-day oscillation of Plaut and Vautard [1994] that exhibits variations in the North Atlantic jet's position and amplitude.

[67] The two leading RC pairs, 1–2 and 3–4, represent our two oscillatory modes. Together, they account for 49% of the variance of the PC-1 time series. Their sum traces well, in general, the excursions of the PC-1 time series that are associated with both high- and low-latitude regime events (Figure 10).

[68] Atmospheric LFO in the Northern Hemisphere (NH) extratropics is characterized by the intermittent occurrence of multiple flow regimes, as well as by low-frequency oscillations (LFOs) that rise above a chaotic background [Ghil, 1987; Ghil *et al.*, 1991; Kimoto and Ghil, 1993b; Itoh and Kimoto, 1999]. We have shown that zonal-flow vacillation in the SH also exhibits both of these complementary aspects. The fairly good, albeit imperfect, correspondence between the regime chronology and the time evolution of the PC-1 reconstruction by the oscillatory components in Figure 10 supports this complementarity between the two different descriptions of LFO [Ghil and Robertson, 2002].

[69] Further examination of the relationship between the zonal-flow regimes and the LFOs in the PC-1 time series shows that the high- and low-latitude regimes are often associated with the slow phases of the 135- and 70-day oscillatory components (Figure 11). By extending certain ideas of successive bifurcation theory [Eckmann, 1981; Ghil and Childress, 1987, chapter 6], Kimoto and Ghil [1993b] hypothesized that some of the observed flow regimes may correspond to slow phases of a destabilized limit cycle, which exists as a stable closed orbit for lower values of certain external parameters. Itoh and Kimoto [1999] examined the relationship between multiple flow regimes and LFOs in the NH. Using an idealized atmospheric model, they presented supporting evidence for the above hypothesis. Our findings about midlatitude zonal-jet dynamics in the SH are also consistent with Kimoto and Ghil's [1993b] hypothesis.

[70] The fact that the two dominant zonal-flow regimes are often associated with the LFOs' slow phases provides hope for improved long-range forecasts of zonal-flow

regimes, contrary to a stochastic view of regime transitions. *Kidson and Watterson* [1999] reported that regression-based forecasts of the high- and low-latitude states achieved only marginal improvements over Markovian decay at intervals of a few days, by inclusion of momentum flux as a predictor.

[71] In Figure 12 we showed that LFO phase information could have some value as a predictor for the extreme phases of zonal-flow vacillation, although rapid transitions between the two are still difficult to locate and predict. The full realization of this promise will require considerably more work that uses advanced statistical, as well as hybrid dynamical-statistical methods [*Ghil*, 1987; *Strong et al.*, 1995; *Ghil and Jiang*, 1998].

### Appendix A: Linear Stochastic Model for the Null Hypothesis

[72] In order to test the statistical significance of the observed PDF, we formulate a null hypothesis that the observed bivariate PC time series cannot be distinguished from a bivariate AR(1) process [*Gardiner*, 1985]. One hundred sets of red-noise time series that have the same length as the original PC time series are generated using the 2-D AR(1) model described below.

[73] Our 2-D AR(1) model takes the form

$$\mathbf{Z}'_i = \Phi \mathbf{Z}'_{i-1} + \mathbf{W}_i, \quad (\text{A1})$$

where the vector red-noise time series  $\mathbf{Z}'_i$ , the autoregressive coefficient matrix  $\Phi$ , and the white-noise shock  $\mathbf{W}_i$  are given by

$$\mathbf{Z}'_i = \begin{pmatrix} z'_{1,i} \\ z'_{2,i} \end{pmatrix}, \Phi = \begin{pmatrix} \phi_{11} & \phi_{12} \\ \phi_{21} & \phi_{22} \end{pmatrix}, \mathbf{W}_i = \begin{pmatrix} w_{1,i} \\ w_{2,i} \end{pmatrix}.$$

Deviations from the time mean are denoted by  $()'$ ; for example,

$$\mathbf{Z}'_i = \mathbf{Z}_i - E(\mathbf{Z}_i),$$

where  $E()$  is the expectation.

[74] The parameters to be estimated in this model are the time mean of the red-noise time series  $E(\mathbf{Z}_i)$ , the autoregressive coefficient matrix  $\Phi$ , and the lag-0 covariance matrix of the white-noise shock  $\Sigma$ . The time mean  $E(\mathbf{Z}_i)$  is estimated from the original PC time series  $\mathbf{X}_i$ ,

$$E(\mathbf{Z}_i) = E(\mathbf{X}_i) = E \begin{pmatrix} x_{1,i} \\ x_{2,i} \end{pmatrix}. \quad (\text{A2})$$

[75] In order to estimate  $\Phi$  and  $\Sigma$  we define the covariance matrix at lag  $k$  of the red-noise time series as follows:

$$\Gamma(k) = \text{Cov}(\mathbf{Z}_i, \mathbf{Z}_{i+k}) = \begin{bmatrix} \gamma_{11}(k) & \gamma_{12}(k) \\ \gamma_{21}(k) & \gamma_{22}(k) \end{bmatrix} = \text{Cov}(\mathbf{Z}_{i-k}, \mathbf{Z}_i).$$

The two diagonal elements of  $\Gamma(k)$  correspond to the autocorrelations, and its two off-diagonal elements account

for the cross-correlations. The covariance matrix  $\Gamma(k)$  of the red noise is also estimated from the original PC time series, as in the time mean estimate, so that the original PC time series and the red-noise time series have the same mean and covariance structure.

[76] From equation (A1) we have

$$E \left[ \mathbf{Z}'_{i-k} \left( \mathbf{Z}'_i{}^T - \mathbf{Z}'_{i-1}{}^T \Phi^T \right) \right] = E \left[ \mathbf{Z}'_{i-k} \mathbf{W}_i^T \right], \quad (\text{A3})$$

where  $()^T$  denotes the transpose of the vector or matrix. From the definition of white noise

$$\text{Cov}(\mathbf{W}_i, \mathbf{W}_{i+k}) = \mathbf{0}, \quad k \neq 0.$$

Using this property, equation (A3) for  $k = 1$  leads to the Yule-Walker equation

$$\Gamma(1) - \Gamma(0)\Phi^T = \mathbf{0}.$$

The Yule-Walker estimate of the autoregressive coefficient matrix  $\Phi$  is given by

$$\Phi = \Gamma^T(1)\Gamma^{-1}(0). \quad (\text{A4})$$

[77] Finally, equation (A3) for  $k = 0$  results in the estimate of the lag-0 covariance matrix of the white-noise shock,

$$\Sigma = \Gamma(0) - \Gamma^T(1)\Phi^T = \Gamma(0) - \Gamma^T(1)\Gamma^{-1}(0)\Gamma(1). \quad (\text{A5})$$

Equations (A2), (A4), and (A5) provide all the parameters needed to define the 2-D AR(1) model of equation (A1).

[78] **Acknowledgments.** We acknowledge the NOAA-CIRES Climate Diagnostics Center, at Boulder, Colorado for providing the NCEP/NCAR Reanalysis data, which is available freely online at <http://www.cdc.noaa.gov>. It is a pleasure to thank two anonymous reviewers for their helpful and constructive comments. This research was supported by NSF Grant ATM 00-82131 (MG), NASA Grant NAG5-7294 (MG), DOE Grant DE-FG03-98ER62615 (AWR), and a Chancellor's Dissertation Year Fellowship at the University of California, Los Angeles (SK).

### References

- Akahori, K., and S. Yoden, Zonal flow vacillation and bimodality of baroclinic eddy life cycles in a simple global circulation model, *J. Atmos. Sci.*, *54*, 2349–2361, 1997.
- Allen, M. R., and L. A. Smith, Monte Carlo SSA: Detecting irregular oscillations in the presence of colored noise, *J. Clim.*, *9*, 3373–3404, 1996.
- Andrews, D. G., and M. E. McIntyre, Planetary waves in horizontal and vertical shear: The generalized Eliassen-Palm relation and the mean zonal acceleration, *J. Atmos. Sci.*, *33*, 2031–2048, 1976.
- Broomhead, D. S., and G. King, Extracting qualitative dynamics from experimental data, *Physica D*, *20*, 217–236, 1986.
- Dettinger, M. D., and M. Ghil, Seasonal and interannual variations of atmospheric CO<sub>2</sub> and climate, *Tellus, Ser. B*, *50*, 1–24, 1998.
- Eckmann, J.-P., Roads to turbulence in dissipative dynamical systems, *Rev. Mod. Phys.*, *53*, 643–654, 1981.
- Edmon, H. J., B. J. Hoskins, and M. E. McIntyre, Eliassen-Palm cross sections for the troposphere, *J. Atmos. Sci.*, *37*, 2600–2616, 1980.
- Fraedrich, K., Estimating the dimensions of weather and climate attractors, *J. Atmos. Sci.*, *43*, 419–432, 1986.
- Fukunaga, K., and L. D. Hostetler, The estimation of the gradient of a density function, *IEEE Trans. Inf. Theory*, *IT-21*, 32–40, 1975.
- Gardiner, C. W., *Handbook of Stochastic Methods*, 442 pp., Springer-Verlag, New York, 1985.
- Ghil, M., Dynamics, statistics, and predictability of planetary flow regimes, in *Irreversible Phenomena and Dynamical Systems Analysis in the Geo-*

- sciences, edited by C. Nicolis and G. Nicolis, pp. 241–283, D. Reidel, Norwell, Mass., 1987.
- Ghil, M., and S. Childress, *Topics in Geophysical Fluid Dynamics: Atmospheric Dynamics, Dynamo Theory, and Climate Dynamics*, 485 pp., Springer-Verlag, New York, 1987.
- Ghil, M., and N. Jiang, Recent forecast skill for the El Niño/Southern Oscillation, *Geophys. Res. Lett.*, *25*, 171–174, 1998.
- Ghil, M., and A. W. Robertson, “Waves” vs. “particles” in the atmosphere’s phase space: A pathway to long-range forecasting?, *Proc. Natl. Acad. Sci.*, *99*, suppl. 1, 2493–2500, 2002.
- Ghil, M., and R. Vautard, Interdecadal oscillations and the warming trend in global temperature time series, *Nature*, *350*, 324–327, 1991.
- Ghil, M., M. Kimoto, and J. D. Neelin, Nonlinear dynamics and predictability in the atmospheric sciences, *Rev. Geophys.*, *36*, 46–55, 1991.
- Ghil, M., et al., Advanced spectral methods for climatic time series, *Rev. Geophys.*, *40*, 10.1029/2000GR000092, in press, 2002.
- Hartmann, D. L., and F. Lo, Wave-driven zonal flow vacillation in the Southern Hemisphere, *J. Atmos. Sci.*, *55*, 1303–1315, 1998.
- Hsu, C. J., and F. Zwiers, Climate change in recurrent regimes and modes of Northern Hemisphere atmospheric variability, *J. Geophys. Res.*, *106*, 20,145–20,159, 2001.
- Itoh, H., and M. Kimoto, Weather regimes, low-frequency oscillations, and principal patterns of variability: A perspective of extratropical low-frequency variability, *J. Atmos. Sci.*, *56*, 2684–2705, 1999.
- Kalnay, E., et al., The NCEP/NCAR 40-year reanalysis project, *Bull. Am. Meteorol. Soc.*, *77*, 437–471, 1996.
- Karoly, D. J., The role of transient eddies in low-frequency zonal variations of the Southern Hemisphere, *Tellus, Ser. A*, *42*, 41–50, 1990.
- Kidson, J. W., Index cycles in the Southern Hemisphere during the Global Weather Experiment, *Mon. Weather Rev.*, *114*, 1654–1663, 1986.
- Kidson, J. W., Indices of the Southern Hemisphere zonal wind, *J. Clim.*, *1*, 183–194, 1988.
- Kidson, J. W., Intraseasonal variations in the Southern Hemisphere circulation, *J. Clim.*, *4*, 939–953, 1991.
- Kidson, J. W., and I. G. Watterson, The structure and predictability of the high-latitude mode in the CSIRO9 general circulation model, *J. Atmos. Sci.*, *56*, 3859–3873, 1999.
- Kimoto, M., and M. Ghil, Multiple flow regimes in the Northern Hemisphere winter, I, Methodology and hemispheric regimes, *J. Atmos. Sci.*, *50*, 2625–2643, 1993a.
- Kimoto, M., and M. Ghil, Multiple flow regimes in the Northern Hemisphere winter, II, Sectorial regimes and preferred transitions, *J. Atmos. Sci.*, *50*, 2645–2673, 1993b.
- Koo, S., Nonlinear aspects of atmospheric zonal-flow vacillation, Ph.D. thesis, 163 pp., University of California, Los Angeles, Calif., 2001.
- Koo, S., and M. Ghil, Successive bifurcations in a simple model of atmospheric zonal-flow vacillation, *Chaos*, *12*, 300–309, 2002.
- Mann, M. E., and J. M. Lees, Robust estimation of background noise and signal detection in climatic time series, *Clim. Change*, *33*, 409–445, 1996.
- Mo, K. C., and M. Ghil, Cluster analysis of multiple planetary flow regimes, *J. Geophys. Res.*, *93*, 10,927–10,952, 1988.
- Moron, V., R. Vautard, and M. Ghil, Trends, interdecadal and interannual oscillations in global sea-surface temperatures, *Clim. Dyn.*, *14*, 545–569, 1998.
- Newton, C. W., (Ed.), *Meteorology of the Southern Hemisphere*, 263 pp., Am. Meteorol. Soc., Boston, Mass., 1972.
- Plaut, G., and R. Vautard, Spells of low-frequency oscillations and weather regimes in the Northern Hemisphere, *J. Atmos. Sci.*, *51*, 210–236, 1994.
- Rossby, C. G., et al., Relation between variations in the intensity of the zonal circulation of the atmosphere and the displacements of the semi-permanent centers of action, *J. Meteorol.*, *2*, 38–55, 1939.
- Silverman, B. W., *Density Estimation for Statistics and Data Analysis*, 175 pp., Chapman and Hall, New York, 1986.
- Simonnet, E., and G. Plaut, Space-time analysis of geopotential height and SLP, intraseasonal oscillations, weather regimes, and local climates over the North Atlantic and Europe, *Clim. Res.*, *17*, 325–342, 2001.
- Strong, C. M., F.-F. Jin, and M. Ghil, Intraseasonal oscillations in a barotropic model with annual cycle, and their predictability, *J. Atmos. Sci.*, *52*, 2627–2642, 1995.
- Thomson, D. J., Spectrum estimation and harmonic analysis, *IEEE Proc.*, *70*, 1055–1096, 1982.
- Thomson, D. J., Quadratic-inverse spectrum estimates: Application to paleoclimatology, *Philos. Trans. R. Soc. London, Ser. A*, *332*, 539–597, 1990.
- Van Loon, H., The half-yearly oscillations in middle and high southern latitudes and the coreless winter, *J. Atmos. Sci.*, *24*, 472–486, 1967.
- Vautard, R., and M. Ghil, Singular spectrum analysis in nonlinear dynamics, with application to paleoclimatic time series, *Physica D*, *35*, 395–424, 1989.
- Vautard, R., B. Legras, and M. Déqué, On the source of midlatitude low-frequency variability, I, A statistical approach to persistence, *J. Atmos. Sci.*, *45*, 2811–2843, 1988.
- Vautard, R., P. Yiou, and M. Ghil, Singular spectrum analysis: A toolkit for short, noisy, chaotic signals, *Physica D*, *58*, 95–126, 1992.
- Watterson, I. G., Southern midlatitude zonal wind vacillation and its interaction with the ocean in GCM simulations, *J. Clim.*, *13*, 562–578, 2000.
- Willett, H. C., Patterns of world weather changes, *Eos Trans. AGU*, *29*, 803–809, 1948.
- Yoden, S., M. Shiotani, and I. Hirota, Multiple planetary flow regimes in the Southern Hemisphere, *J. Meteorol. Soc. Japan*, *65*, 571–585, 1987.

---

M. Ghil, S. Koo, and A. W. Robertson, Department of Atmospheric Sciences and Institute of Geophysics and Planetary Physics, University of California, Los Angeles, Los Angeles, CA 90095-1565, USA. (ghil@atmos.ucla.edu; koo@mail.nih.gov; awr@iri.columbia.edu)